Eur. Phys. J. B (2016) 89: 107
DOI: 10.1140/epjb/e2016-70001-3

THE EUROPEAN PHYSICAL JOURNAL B

Regular Article

# Electron and donor-impurity-related Raman scattering and Raman gain in triangular quantum dots under an applied electric field

Anton Tiutiunnyk[1,2], Volodymyr Akimov[1,2,3], Viktor Tulupenko[1,2], Miguel E. Mora-Ramos[4], Esin Kasapoglu[5], Alvaro L. Morales[1], and Carlos Alberto Duque[1,a]

[1] Grupo de Materia Condensada-UdeA, Instituto de Física, Facultad de Ciencias Exactas y Naturales, Universidad de Antioquia UdeA, Calle 70 No. 52-21, Medellín, Colombia
[2] Department of Physics, Donbass State Engineering Academy, Shkadinova 72, 84313 Kramatorsk, Ukraine
[3] Universidad de Medellín, Carrera 87 No. 30-65, Medellín, Colombia
[4] Centro de Investigación en Ciencias, Instituto de Investigación en Ciencias Básicas y Aplicadas, Universidad Autónoma del Estado de Morelos, Av. Universidad 1001, CP 62209 Cuernavaca, Morelos, Mexico
[5] Cumhuriyet University, Physics Department, 58140 Sivas, Turkey

Received 2 January 2016 / Received in final form 12 February 2016
Published online 20 April 2016 – 

**Abstract.** The differential cross-section of electron Raman scattering and the Raman gain are calculated and analysed in the case of prismatic quantum dots with equilateral triangle base shape. The study takes into account their dependencies on the size of the triangle, the influence of externally applied electric field as well as the presence of an ionized donor center located at the triangle's orthocenter. The calculations are made within the effective mass and parabolic band approximations, with a diagonalization scheme being applied to obtain the eigenfunctions and eigenvalues of the $x$-$y$ Hamiltonian. The incident and secondary (scattered) radiation have been considered linearly-polarized along the $y$-direction, coinciding with the direction of the applied electric field. For the case with an impurity center, Raman scattering with the intermediate state energy below the initial state one has been found to show maximum differential cross-section more than by an order of magnitude bigger than that resulting from the scheme with lower intermediate state energy. The Raman gain has maximum magnitude around 35 nm dot size and electric field of 40 kV/cm for the case without impurity and at maximum considered values of the input parameters for the case with impurity. Values of Raman gain of the order of up to $10^4\,\mathrm{cm}^{-1}$ are predicted in both cases.

## 1 Introduction

With the advances of nanotechnology engineering, new opportunities of growing low-dimensional heterostructures of various kinds and geometries, with pre-determined physical properties, have arisen. Since the 90s the fabrication and theoretical study of quantum dots (QDs) of different shapes besides the originally treated circular and squared ones. In this sense, configurations like triangular, oval, semicircular, elliptical, etc. have been reported [1,2]. Nowadays QDs of even more complicated geometries are often created like, for example, the sagittal pyramid case [3]. This opens more and more new possibilities in developing materials or systems with the desired physical properties.

From the point of view of practical realisation it is possible to mention reports on metallic, dielectric and semiconducting nanostructures bearing triangular geometry [4–8]. In particular, references [7,8] reported the fabrication of a thin GaAs QDs with shape of equilateral triangle grown on a GaAs (111) substrate by droplet epitaxy technique. The structures that shall be investigated in the present article are very similar to these latter QDs both in shape and size.

From the times of the detection of the stimulated Raman scattering [9] – one of the first effects of nonlinear optics discovered – and the first continuous-wave Raman laser [10], the problem of obtaining efficient Raman lasing still remains as both a fundamental and technological challenge despite a number of perspective applications. The development of semiconductor nanostructure technologies opens new horizons since low-dimensional systems allow overcoming the traditional contradiction between gain and bandwidth for Raman lasers [11]. Therefore the problem of Raman scattering in 2- , 1-, and 0-dimensional structures, including semiconductor quantum dots [11–13], constitutes a subject of top interest in contemporary solid-state physics.

[a] e-mail: cduque@fisica.udea.edu.co

In previous works we have studied the 2D Schrödinger problem for the case of a 3-fold symmetrical system (i.e., that with 3 axis of symmetry) applied to some semiconductor nanostructures in order to investigate their energy structure and optical properties. Namely, in the report of reference [14] the eigenvalues and eigenfunctions for the triangular QD have been numerically obtained and linear and non-linear intersubband absorption coefficient and refractive index changes were calculated. Afterwards we studied the electronic and optical properties of a system of 3-coupled quantum well wires with triangular cross-sections [15]. Here our aim is to calculate and analyse intersubband optical properties of the triangular QD connected to electron Raman scattering. We are interested in discussing the effects of the variation in QD size, the application of an in-plane external electric field and the presence of an ionized donor center placed at the orthocenter of the triangle.

The article is organized as follows: in Section 2 we give some key elements of the theoretical model employed. Section 3 is devoted to present and discuss the obtained results and Section 4 contains the conclusions of the work.

## 2 Theory framework

### 2.1 Potential model and Hamiltonian

The model system considered in this work is a prismatic GaAs QD with the base in the form of an equilateral triangle of side $L$ – taken to lie in the $(x, y)$ plane – in a $Al_{0.3}Ga_{0.7}As$ bulk environment. According to data on QD height reported in references [7,8] (where GaAs/AlGaAs QDs were grown by Stranski-Krastanov method), and [16] (with the using of droplet epitaxy), we can talk about the possibility of practical realization of triangular QDs with vertical size of 2 nm. In this case the QD can be considered to be practically flat; because lateral size is significantly larger than the height. Besides, dimensions along the $z$-direction are insufficient for quantization of more than one level in the energy of the vertical motion. Accordingly, coordinates $z$ and $(x, y)$ can be separated so the problem actually becomes a two-dimensional one.

For the sake of the numerical procedure, the whole system is put inside a big prismatic rectangular quantum box with the dimensions $L_x \times L_y \times h$ (with $h = 2\,\text{nm}$ is the height of the QD) and infinite potential outside the box (the $x$-$y$ projection of the prismatic QD system structure is schematically depicted in Fig. 1).

In addition, an ionized donor impurity center is placed at the orthocenter of the triangle whereas an electric field $F$ is applied along the $y$-axis, choosing one of the triangle's side to be parallel to the $x$-axis. The zero potential energy value corresponds to the conduction band edge of GaAs.

The Hamiltonian of our model, correspondingly, is:

$$H = -\frac{\hbar^2}{2\,m^*}\,\nabla^2 + V_1(x,y) + V_2(z) - e\,F\,y - \frac{\kappa\,e^2}{\varepsilon\,r}, \quad (1)$$

where $m^*$ is the electron effective mass, $e$ is the carrier charge, $\varepsilon$ is the dielectric constant – taken to be the same for both materials – $r \cong \sqrt{x^2+y^2}$ is the distance from the impurity center – assumed to have coordinates $(0, 0, 0)$-, and $V_1(x, y)$ is the in-plane confining potential with values 0, $V_0$, and $\infty$ depending on the specific region (see Fig. 1). The potential $V_2(z)$ is defined as zero for $|z| \leq h/2$ and infinite elsewhere. The $\kappa$-parameter in the last term at the right-hand side refers to the fact that we considered both cases with $(\kappa = 1)$ and without $(\kappa = 0)$ ionized impurity center. At this point it is worth saying that our assumption of a strictly two-dimensional Coulombic interaction term in (1) is justified by numerical estimation. We have verified that the use of a 3D electron-impurity distance only changes the energy state values in 1% and since there is a – nearly – rigid shift of the spectrum, the transition energies are modified only in a 0.1%. In consequence, the system behaves essentially as a 2D one.

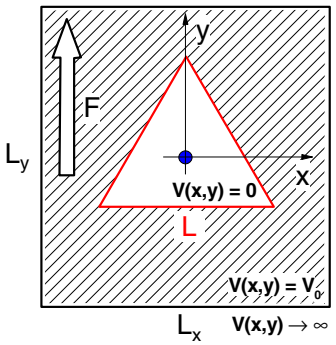


**Fig. 1.** The model of the equilateral triangle QD. Triangle side is $L$. Potential inside the triangle area corresponds to GaAs conduction band. The region outside the triangle is of $Al_{0.3}Ga_{0.7}As$. The potential outside the rectangular area $L_x \times L_y$ is considered as an infinite. The electric field $F$ is directed along $y$-direction. Donor impurity center is positioned at the orthocenter of the triangular area.

Taking into account that $h \ll L$ we use the adiabatic approximation in order to find the eigenfunctions and eigenvalues of equation (1). In this case the 3D wave function $\Upsilon(x, y, z)$ is written as the multiplication of the in-plane function $[\Psi(x, y)]$ times the axial function $[g(z)]$. That is, $\Upsilon(x, y, z) = N\,\Psi(x, y)\,g(z)$, where $N$ is the normalization constant. The $g(z)$ function is the solution of the differential equation

$$\left[-\frac{\hbar^2}{2\,m^*}\,\frac{\partial^2}{\partial z^2} + V_2(z)\right]\,g(z) = E_z\,g(z). \quad (2)$$

The following step is to use the first axial subband $E_z^1$ energy (which is constant in this work due to the constant value of the height of the dot, $h$), as the adiabatic potential and to write the eigenvalues equation for the $[\Psi(x, y)]$ function in the form:

$$\left[-\frac{\hbar^2}{2\,m^*}\,\nabla^2 + \widetilde{V}(x,y)\right]\,\Psi(x,y) = E\,\Psi(x,y), \quad (3)$$

where $\widetilde{V}(x,y) = V_1(x,y) - e\,F\,y - \frac{\kappa\,e^2}{\varepsilon\,r} + E_z^1$.

The eigenvalues $E_0$, $E_1$, $E_2, \ldots$ and eigenfunctions $\Psi_0$, $\Psi_1$, $\Psi_2$, $\ldots$ of the 2D problem in equation (3) have

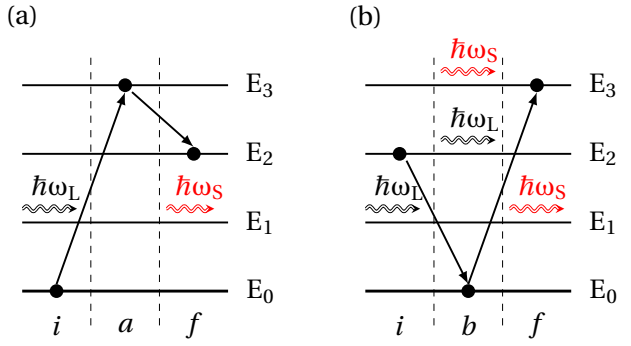


**Fig. 2.** Schematic representation of energy levels and considered transition between them. Panel (a) shows process of absorption of incident resonant photon with following emission of the secondary photon. Panel (b) shows the process of initial emission of secondary photon and subsequent absorption of incident resonant photons.

been found numerically by means of 2D Fourier expansion within the big rectangular quantum box as it is described in [14,15]. To construct the expansion basis we take the lowest 50 values of the quantum numbers for the quantum box states along the $x$ and $y$ dimensions. Sorting the corresponding energies in ascending way, we selected the set of first 400 values. This choice provides both enough calculation speed and accuracy. It should also be said that triangle size range of $L$ is chosen so that at least we had three excited energy states (in the case of 25 nm), looking for keeping a not too small distance between the levels (40 nm). The values of $L$ were changed in increments of 1 nm, which approximately corresponds to twice the length of the crystal lattice unit cell for GaAs.

### 2.2 Raman scattering theory

To study Raman scattering we have considered the lowest 4 energy levels. As mentioned, the range of triangle side $L$ is taken from 25 to 40 nm, just to ensure the presence of the at least 4 levels confined inside the QD. On the other hand, our calculations show that the outer box size variations does not have essential influence on the level positions for the whole range of $L$.

As was shown in our previous work (see Figs. 2 and 3 in Ref. [14],) the wave functions for the equilateral triangle QD are symmetric with respect to $y$-axis for the states $\Psi_0$, $\Psi_2$ and $\Psi_3$ and anti-symmetric for the state $\Psi_1$. This follows the general trend for the 3-fold symmetry systems discussed in reference [17]. The applied electric field – along the $y$-direction – does not remove this kind of symmetry, therefore the electron-light interaction matrix elements for all the combinations including the first excited state within our 4-level problem turn to zero. In accordance, the symmetry of the systems prohibits all the transitions from/to the 1st state and even prohibits using it as an intermediate state. This means that the included transitions will be: $0 \to 3 \to 2$ (see Fig. 2a – first type transition) and $2 \to 0 \to 3$ (see Fig. 2b – second type transition). Moreover, for both transitions the incident light photon energy should be equal to $\hbar\omega_L = E_3 - E_0$, and the secondary radiation will have a maximum at $\hbar\omega_S = E_3 - E_2$ for the first type transition and at $\hbar\omega_S = E_2 - E_0$ for the second one.

Each process can be divided into initial, intermediate and final states, with corresponding subscripts $i$, $a(b)$, and $f$:

$$\begin{aligned} E_i &= E_0 + \hbar\omega_L, \quad & E_i &= E_2 + \hbar\omega_L, \\ E_a &= E_3, & E_b &= E_0 + \hbar\omega_L + \hbar\omega_S, \\ E_f &= E_2 + \hbar\omega_S, & E_f &= E_3 + \hbar\omega_S, \end{aligned} \tag{4}$$

where first the column is for Figure 2a and the second column is for Figure 2b.

The expression for the electron Raman differential cross-section (DCS), for processes 2a and 2b, respectively, is given by [18–22]

$$\left.\frac{d^2\sigma}{d\Omega\, d\omega_S}\right|_{iaf,ibf} = \frac{V^2\, n(\omega_S)}{8\,\pi^3\, c^4\, n(\omega_L)}\,\omega_S^2 \times \frac{2\pi}{\hbar}\left|\frac{T_{iaf,ibf}}{E_i - E_{a,b} + j\,\Gamma}\right|^2 \delta\left(E_f - E_i\right), \tag{5}$$

where $T_{iaf} = \langle\Psi_f|H_S|\Psi_a\rangle\,\langle\Psi_a|H_L|\Psi_i\rangle$ and $T_{ibf} = \langle\Psi_f|H_L|\Psi_b\rangle\,\langle\Psi_b|H_S|\Psi_i\rangle$, where $c$ is the light speed in vacuum, $n(\omega)$ is the refraction index depending on the radiation frequency, $V$ is a volume of the structure. Indexes $L$ and $S$ refer to the incident light and emitted secondary radiation correspondingly. Besides, $j = \sqrt{-1}$ and $\Gamma$ is a broadening of the corresponding levels due to the lifetime (here we choose $\Gamma = 1$ meV) [23]. In our calculations we have considered the case of both incident and Raman radiation polarized along $y$-axis. Under such a configuration the electron-photon interaction operator is:

$$H_k = -\frac{|e|}{m^*}\sqrt{\frac{2\,\pi\,\hbar}{V\,\omega_k}}\left(j\,\hbar\frac{\partial}{\partial y}\right), \tag{6}$$

where $k = S, L$.

Replacing Dirac delta-function by the Lorentzian with broadening given by $\Gamma$ we finally get the expression for DCS as:

$$\left.\frac{d^2\sigma}{d\Omega\, d\omega_S}\right|_{iaf,ibf} = \frac{C_1}{\pi}\frac{\omega_S}{\omega_L}\,\frac{|\widetilde{T}_{iaf,ibf}|^2}{(E_i - E_{a,b})^2 + \Gamma^2}\,\frac{\Gamma^2}{(E_f - E_i)^2 + \Gamma^2}. \tag{7}$$

Here $\widetilde{T}_{iaf} = M_{fa}\,M_{ai}$ and $\widetilde{T}_{ibf} = M_{fb}\,M_{bi}$, with $M_{mn} = \langle\Psi_m|\frac{\partial}{\partial y}|\Psi_n\rangle$ being the matrix elements,

$$C_1 = \frac{n(\omega_S)}{n(\omega_L)}\,\frac{\hbar}{c^4}\left(\frac{|e|\hbar}{m_e^*}\right)^4 \tag{8}$$

assuming $n(\omega_{S(L)}) = n = \text{const.}$, $C_1 = \text{const}$. It is worth pointing out that the results for DCS below will be presented in arbitrary units so the constant multiplier is

not of importance. The maximum amplitude for the DCS given by equation (7) is reached for secondary radiation photon energies fulfilling the following conditions: (i) the usually named as step-like energy, in which $\hbar\omega_S = E_{sl}$ with $|E_f - E_i| \to 0$ and (ii) the resonant-like energy $\hbar\omega_S = E_{rl}$, when $|E_i - E_{a,b}| \to 0$.

### 2.3 Raman gain theory

The third order nonlinear susceptibility due to electron Raman scattering, and associated with the process in Figure 2a, is [24]:

$$\chi^{(3)}(\omega_S;\omega_L,\omega_S,-\omega_L) = \frac{(N_f - N_i)\, e^4\, |\langle\Psi_f|y|\Psi_a\rangle|^2\, |\langle\Psi_a|y|\Psi_i\rangle|^2}{\varepsilon_0\, |E_a - E_i - j\Gamma|^2 (E_f - E_i - j\Gamma)} \quad (9)$$

where $N_f$ and $N_i$ are the occupation numbers of the corresponding states.

After some manipulations, the final equation (9) becomes:

$$|\chi^{(3)}(\omega_S;\omega_L,\omega_S,-\omega_L)| = \sqrt{(E_f - E_i)^2 + \Gamma^2} \times \left| \frac{-\rho\, e^4\, |D_{ia}|^2\, |D_{af}|^2}{\varepsilon_0\, [(E_a - E_i)^2 + \Gamma^2]\, [(E_f - E_i)^2 + \Gamma^2]} \right| \quad (10)$$

where $D_{mn} = \langle\Psi_m|y|\Psi_n\rangle$ are the electric dipole matrix elements and $\rho\ (= 1/(L_x \times L_y \times h) = 1.4 \times 10^{25}\,\mathrm{m}^{-3})$ is the low temperature electron density in the ground state.

Then, knowing that the Raman gain depends of the nonlinear susceptibility as

$$G_R = -\frac{\omega_S}{n\, c}\, \mathrm{Im}(\chi^{(3)})\, |A|^2\,, \quad (11)$$

where $|A|^2$ – is a magnitude of the electric field of an incident radiation, and expressing $|A|^2$ through intensity $I$ as $|A|^2 = \frac{2\,I}{n\,\epsilon_0\,c}$ (with refractive index $n = \sqrt{\varepsilon_r}$) we finally arrive to

$$G_R = \frac{2\, I\, \hbar\omega_S}{c^2\, \varepsilon_r\, \varepsilon_0^2\, \hbar}\, \frac{\rho\, e^4\, |D_{ia}|^2\, |D_{af}|^2}{\Gamma^3}. \quad (12)$$

## 3 Results and discussion

Before we begin discussing the results, it is necessary to set clear the set of parameters of the system that define the configuration considered. The outer box size is $L_x \times L_y = 60\,\mathrm{nm} \times 60\,\mathrm{nm}$. The effective electron mass is $m^* = 0.0665 m_0$ (where $m_0$ is the free electron mass) [25], and the dielectric constant $\varepsilon_r = 12.35$ [14,26]. Our calculation assumes that the effective masses and dielectric constants are the same for both GaAs and AlGaAs. This is a fairly good approximation in cases where the Al molar fraction is small. The material conduction band discontinuity is $V_0 = 0.6\,(1155.0\,x + 370.0\,x^2) = 227.88$ meV,

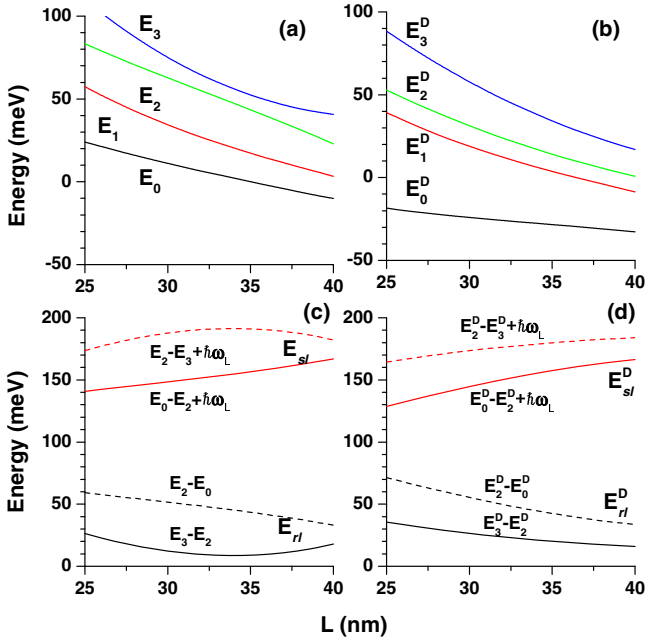


**Fig. 3.** Energy as function of triangle size $L$ in the case without (a) and with impurity (b) localized in the centre. Electric field is directed to $y$-axiz and $F = 60$ kV/cm. The energy levels are referred with respect to the $E_z^1$ energy. (c) and (d) are the graphics of the resonant-like energy $E_{rl}$ (black line) and the step-like energy $E_{sl}$ (red line), for 1-st type transition (see Fig. 2a) solid line, and 2-nd type transition (see Fig. 2b) dashed line.

where $x$ is Al content ($x = 0.3$ in the present work). As mentioned, following [23] for all the values of broadening we have taken 1.0 meV. The intensity of the $y$-oriented electric field is taken to reach up to 80 kV/cm. There are experimental evidences of the possibility of achieving a lateral electric field with such a big magnitude (see, for example, Refs. [27–29]).

### Raman scattering DCS

Figures 3a and 3b show the energy positions of the lowest four energy levels as functions of the triangle side $L$. Zero energy corresponds to the conduction band edge at the orthocenter of the triangle. Figure 3a contains the case without ionized impurity and DC electric field $F = 60$ kV/cm. Figure 3b corresponds to the situation with a ionized impurity on (upper index $D$ refers to ionized donor). With increasing QD size the energy levels naturally go down, due to the reduction of carrier confinement. Additionally, it is possible to notice that with the fall in the degree of confinement, there is generally a decrease in the transition energy between different levels, with the exception of some particular situations like the energy difference between levels 2 and 3, in the case without impurity ($\kappa = 0$), where adjacent states are repulsed (see Fig. 3a). In fact, there is a kind of anti-crossing between 2nd and 3rd levels which is discussed below in the comments to the next figure.

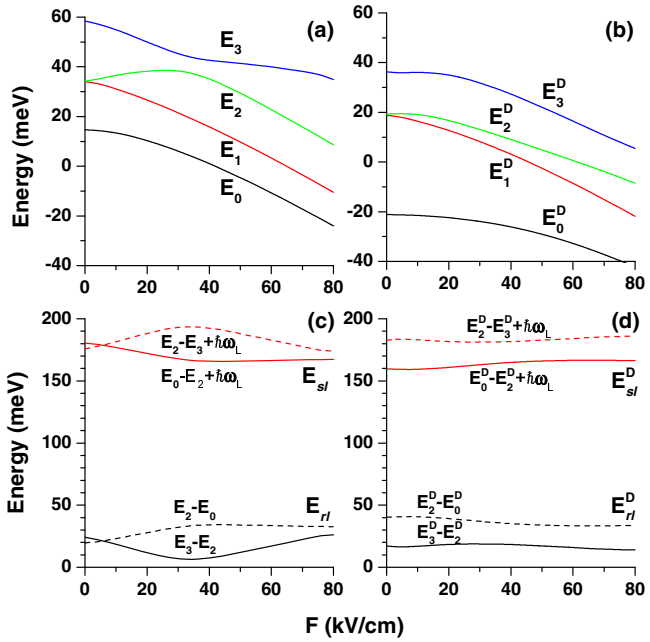


**Fig. 4.** Energy as function of variation of the applied electric field $F$ in the case without (a) and with impurity (b) localized in the orthocentre of the triangle, with $L = 40$ nm. The results in (c) and (d) are the same to Figure 3.

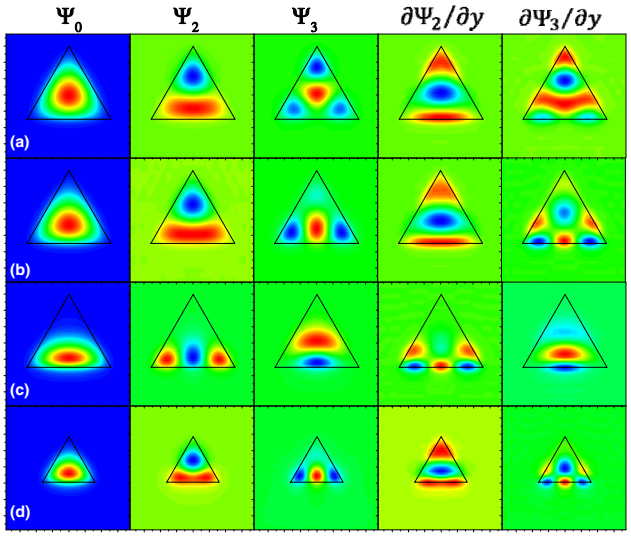


**Fig. 5.** Density plots of the wave functions and their derivatives over $y$-coordinates for the cases of: (a) row – $L = 40$ nm, $F = 0$; (b) row – $L = 40$ nm and $F = 8$ kV/cm; (c) row – $L = 40$ nm, $F = 60$ kV/cm; (d) row – $L = 25$ nm, $F = 60$ kV/cm. No ionized impurity.

Figures 3c and 3d show the variation of the peak energies for two considered transitions (step-like and resonant-like structures) as functions of the triangle size. The incident radiation frequency was selected in a way that guarantees the transition $E_0 \rightarrow E_3$, so $\hbar\omega_L = 200$ meV. Similar incident photon energy for the Raman scattering was considered in reference [30] and experimentally was used in reference [31] for an optically pumping of intersubband laser. The general trend is to increase the step-like energy with QD size because the difference between energies decreases, and with the same $\hbar\omega_L$ a higher energy should be emitted for the electron in order to reach the final state. The resonant-like energy generally decreases as it is a mere difference between energy levels. The exceptional non-monotonic behavior $E_{rl}$ for the first type transition and $E_{sl}$ for the second type transition in the $\kappa = 0$ case is due to the anti-crossing mentioned above.

The graphics appearing in Figure 4 are organized as in the previous one. It contains the dependencies of the same quantities on the value of the externally applied electric field intensity. Notice that when $F = 0$ the first and second excited states are degenerated [17] and their superposition has three-fold symmetry. As expected, the electric field removes the degeneracy so that the energy of the first excited state – which has the anti-symmetric wave function with respect to the $y$ axis (see [14], Figs. 2 and 3) – goes down in energy and that of the second excited state – with symmetric wave function- initially goes up. The latter state, in the $\kappa = 0$ case, forms a kind of anti-crossing point with the third excited state at a field strength about 30–40 kV/cm whose effects can be seen also in Figures 3a and 3c. For the case with impurity ($\kappa = 1$), the splitting is not as large as when $\kappa = 0$, and no anti-crossing is formed within the considered range of the applied electric field although the distance between second and third excited states decreases with $F$. As for the peak energies, for $\kappa = 0$ case they have a change of behaviour around the point of anti-crossing as all of them involve the states labeled as 2 and 3. Meanwhile, for the $\kappa = 1$ case their variations show a flatter character and can be viewed as constants in a first approximation.

In Figure 5 one may observe the density plot of the wave functions (WFs) and their derivatives for some of our allowed states. With electric field increasing from 0 to 60 kV/cm and $L = 40$ nm, the potential in the upper corner of the triangle raises up due to electric field influence. The system looses its 3-fold symmetry leaving only one axis of symmetry, namely $y$-axis. So, in the limit of higher fields it starts resembling a symmetrical quantum well confined along the $x$-direction. This process pushes up to higher energies the confined state with a probability density that have 2 maxima, centered at $y$ axis. In consequence, WFs $\Psi_2$ and $\Psi_3$ exchange their order (compare $\Psi_2$ in Fig. 5a and $\Psi_3$ in Figs. 5b and 5c). Instead, the WF with four local extrema ($\Psi_3$ in Fig. 5a) looses one upper extremum and resembles a WF of the 2nd excited state confined in one dimension. This exchange of mutual position in energy is reflected in Figure 4 like an anticrossing, of which we have already talked about. For the smaller QD side of $L = 25$ nm (Fig. 5d) the increment of the potential in the upper corner associated to the electric field is smaller, so the position exchange does not takes place at $F = 60$ kV/cm. The presence of an ionized impurity center also slows down that process as can be seen from Figure 6, where the mentioned exchange does not occur – at $F = 60$ kV/cm – either; because it creates a kind of potential "crater" out of the lower edge of the triangle and

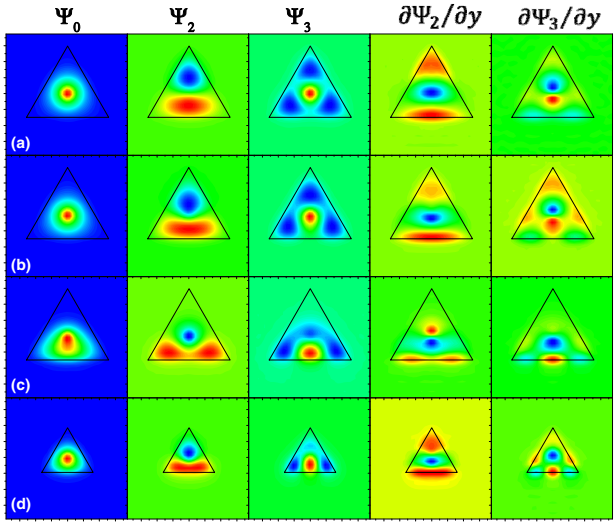


**Fig. 6.** The same as Figure 5 for the case with ionized impurity center in the orthocenter of the triangle.

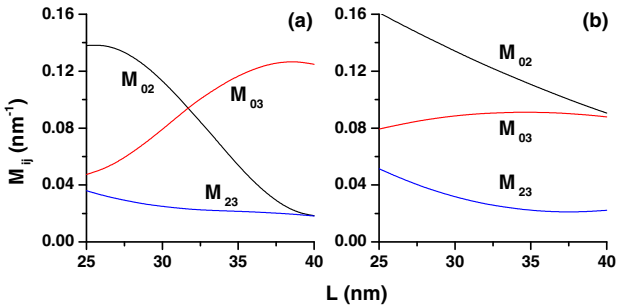


**Fig. 7.** Matrix element $M_{mn}$ as function of triangle size $L$ in the case without (a) and with impurity (b) localized in the orthocentre of the triangle. The electric field is directed to $y$-axis and $F = 60\,\mathrm{kV/cm}$.

thus prevents migrating the whole system to the scheme of one-dimensional confinement.

Figures 7 and 8 show the behaviour of the electron-photon matrix elements used in equation (5) in a simplified form $M_{ij} = \langle \Psi_i | \frac{\partial}{\partial y} | \Psi_j \rangle$, depending on the QD size (with $F = 60\,\mathrm{kV/cm}$), and as functions of the applied electric field (with $L = 40\,\mathrm{nm}$), respectively. It must be kept in mind that for the first-type transition the squared product of $M_{03}$ and $M_{32}$ is used whereas for the second-type one $M_{20}$ and $M_{03}$ are used. Increasing the size of QD leads to a strong increment of $M_{03}$, a strong decrease of $M_{02}$ and a moderate decrease of $M_{23}$. Electric field in its turn has the same qualitative effect. Notice that $M_{03}$ at low electric field starts from 0 or almost 0. The addition of an ionized impurity center keeps the general tendency for both kinds of dependencies, but makes them less pronounced.

This kind of behaviour becomes clear from our previous analysis about the transformation of the system symmetry and WFs. Matrix elements between the ground state WF and WF with two extreme aligned along the $y$-axis are the largest ones. This is due to the fact that the

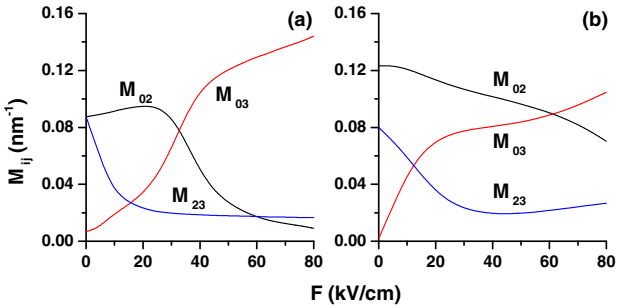


**Fig. 8.** Matrix elements $M_{mn}$ as function of the applied electric field $F$ with $L = 40\,\mathrm{nm}$. In (a) the results are without impurity effects, whereas in (b) there is a donor impurity localized at the orthocentre of the triangle.

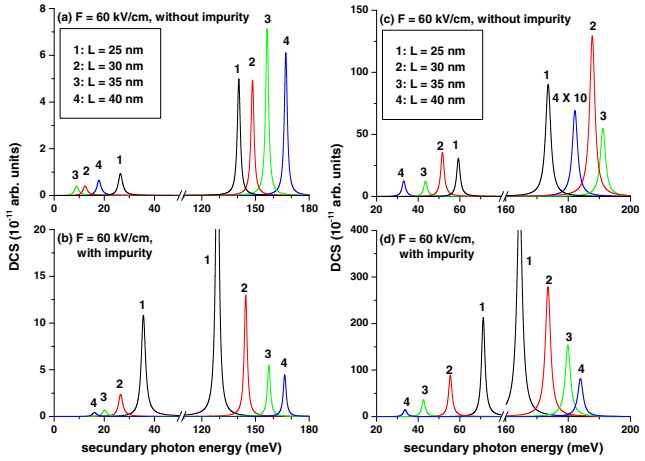


**Fig. 9.** Differential cross-section as function of secondary photon energy in case without impurity (a,c) and with impurity (b,d). First-type transition case in (a,b) and second-type transition case in (c,d). Electric field is $F = 60\,\mathrm{kV/cm}$. Several values of the size of triangle have been considered. Calculations are for $\hbar\omega_L = 200\,\mathrm{meV}$. The resonant-like and step-like peaks are shown on the left- and on the right-hand sides of the energy scale in each of the plots (before and after the break on the energy axis).

derivative of the latter has the biggest maximum spatially coinciding with the maximum of the former (see Figs. 5 and 6). So when the WFs exchange their positions in energy, the magnitude of the matrix elements is exchanged too; something that we can see especially well from the field and size dependencies in the $\kappa = 0$ case.

Figures 9 and 10 show the DCS of the Raman scattering plotted versus the secondary photon energy. With our chosen values of $\Gamma$ the spectra represent a series of separated peaks with their positions corresponding to step-like and resonant-like energy (see Figs. 3 and 4) and their magnitudes proportional to the square product of matrix elements – shown in Figures 7 and 8 – and to $\omega_S$.

Figure 9 provides a series of curves for different values of triangle side $L$ for fixed electric field strength $F$ =60 kV/cm, whilst Figure 10 depicts the case in which the field intensity is varied for a QD with $L = 40\,\mathrm{nm}$.

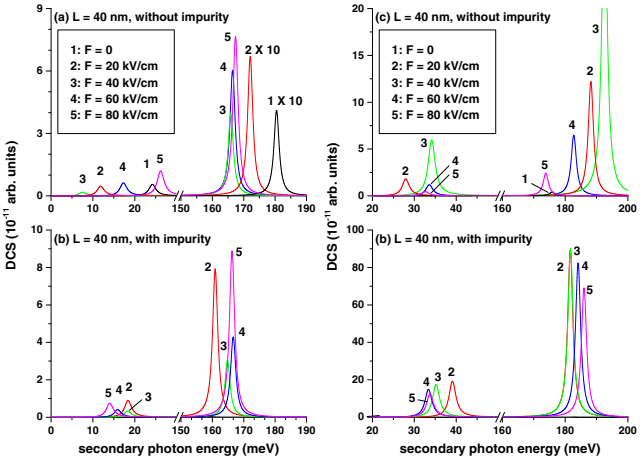


**Fig. 10.** Differential cross-section as function of secondary photon energy in case without impurity (a,b) and with a donor impurity localized at the orthocentre of the triangle (b,d). First-type transition case in (a,b) $\Psi_0 \rightarrow \Psi_3 \rightarrow \Psi_2$ and second-type transition case in (c,d) $\Psi_2 \rightarrow \Psi_0 \rightarrow \Psi_3$. The size of triangle is $L = 40\,\text{nm}$. Several values of the applied electric field have been considered. Calculations are for $\hbar\omega_L = 200\,\text{meV}$. The resonant-like and step-like peaks are shown on the left- and on the right-hand sides of the energy scale in each of the plots (before and after the break on the energy axis).

The DCS is provided in arbitrary units, which are the same for all graphs in both figures so they can be compared. The resonant-like peak magnitude expectedly correlates with the step-like peak being several time less. The biggest – in amplitude – expression of Raman effect is found for the smallest QD of $L = 25\,\text{nm}$ at $F = 60\,\text{kV/cm}$ for the second type transitions, with the presence of the impurity center. That is precisely the configuration in which both matrix elements $M_{02}$ and $M_{03}$ have biggest magnitude (see Fig. 7).

Since the maximum peak values for electric field intensities of 20 and 40 kV/cm occur when $L = 40\,\text{nm}$ in the corresponding section of Figure 10, it will be possible to expect even somewhat bigger values of DCS for the same fields in case of $L = 25\,\text{nm}$ as well. Further decrease of QD size would push the third level to the continuous spectrum so the QD would have less than three confined levels and that makes the effect of described Raman scattering impossible.

Now if we compare DCS corresponding to the two types of scattering for our configuration, the second-type transition effect provides a Raman scattering several times more intense. However, it should be noticed that in our calculations we have not account for the electron distribution, assuming that the initial state is occupied and the final is empty. That allowed us to excluding the temperature and the Fermi level position of the particular structure and consider the most general case. Allowing for a more realistic situation of the equilibrium distribution with some electrons, the temperature would make corrections to the mutual probabilities of the two types of transitions thus decreasing the effectiveness of the type 2 scattering. This happens because the ground state $E_0$ (initial for the type 1) statistically is more likely to be occupied than second excited one, $E_2$, (initial for the type 2). Nevertheless, at higher temperatures type 2 emission can be even more detectable than type 1 due to the bigger DCS.

Another important conclusion is that the presence of the ionized impurity center increases drastically the Raman effect in our QD for all calculated cases. And last but not least, the scattering without electric field is very small in comparison with the one with the electric field so one can say that the electric field switches on the whole mechanism, which works most effectively (has a maximum) around 20–60 kV/cm, depending on the remaining parameters.

In this study, the Raman gain is calculated in the low temperature ($T \sim 0$) approximation with only ground states occupied by the electrons, so we only consider first-type transitions. Unlike we did for obtaining the Raman DCS, here we took a different incident photon energy value, which is exactly equal to the energy difference between the third excited and the ground confined states. Therefore, the process does not need *phonons* taking part in the scattering: $\hbar\omega_L = E_3 - E_0$. Thus the calculation was made for 16 values of incident photon energies, with each being conditioned by the sizes of QDs (4 sizes considered), values of electric fields (4 values considered) and by the presence or absence of impurity in the QDs. All these energies are in the range $(40, 106)$ meV.

Incident laser intensity was taken as $I = 1\,\text{MW/cm}^2$ for all mentioned incident photon energies. The value of $\hbar\omega_S$ in equation (12) was taken as at resonant-like peak (different for each point). The results are presented in Figures 11 and 12. Expectedly, Raman gain behaviour (Figs. 11c, 11f, 12c and 12f) repeats that of the squared product of dipole matrix elements (Figs. 11a, 11d, 12a and 12d). Interestingly enough, the maximum of the third-order optical susceptibility in all our cases corresponds to the minimum energy of Raman photon (Figs. 11b, 11e, 12b and 12e) and the difference is large enough (mind logarithmic scale) to not be compensated by the multiplier $\hbar\omega_S$ in equation (12). The $\kappa = 0$ case clearly shows a maximum gain for a QD size having $L \approx 36\,\text{nm}$, with a lateral electric field perpendicular to one of triangle sides $F = 40$ kV/cm . This points at an important role played by QD geometry and dimensions at the time of looking for a possible application to inter-state Raman devices. It is worth highlighting that its magnitude of $\sim 27 \times 10^3\,\text{cm}^{-1}$ is significantly higher than the one obtained in the case of a GaAs-based intersubband Raman laser which is of the order of $4 \times 10^2\,\text{cm}^{-1}$ [32]. The supposed lasing frequency corresponds to the photon energy of 10 meV, which belongs to the Terahertz region. Of course, in a more realistic environment including finite temperature and statistically determined electron population these figures will change; but nevertheless one would expect the Raman gain to result quite larger than the obtained in quantum wells.

In the case with a ionized impurity, the gain monotonically increases with QD size up to the limiting values. In the scale versus electric field it has a local maximum at

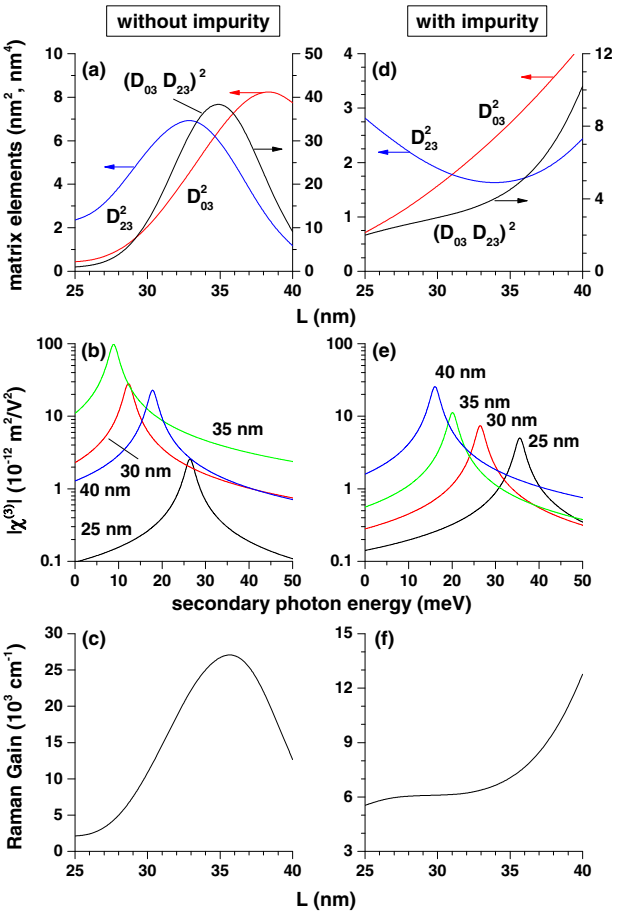


**Fig. 11.** Dipole matrix element as a function of QD size (a,d); the absolute value of the third-order nonlinear optical susceptibility as a function of secondary photon energy at $F = 60$ kV/cm for several values of the QD size (b,e), and Raman gain as function of QD size (c, f). Left panel (a,b,c) is the case without impurity and right panel (d,e,f) corresponds to the case with ionized impurity center. In (b, c, e, f) the incident poton energy corresponds to $\hbar\omega_L = E_3 - E_0$. In (c, f) the secondary photon energy corresponds to $\hbar\omega_S = E_3 - E_2$.

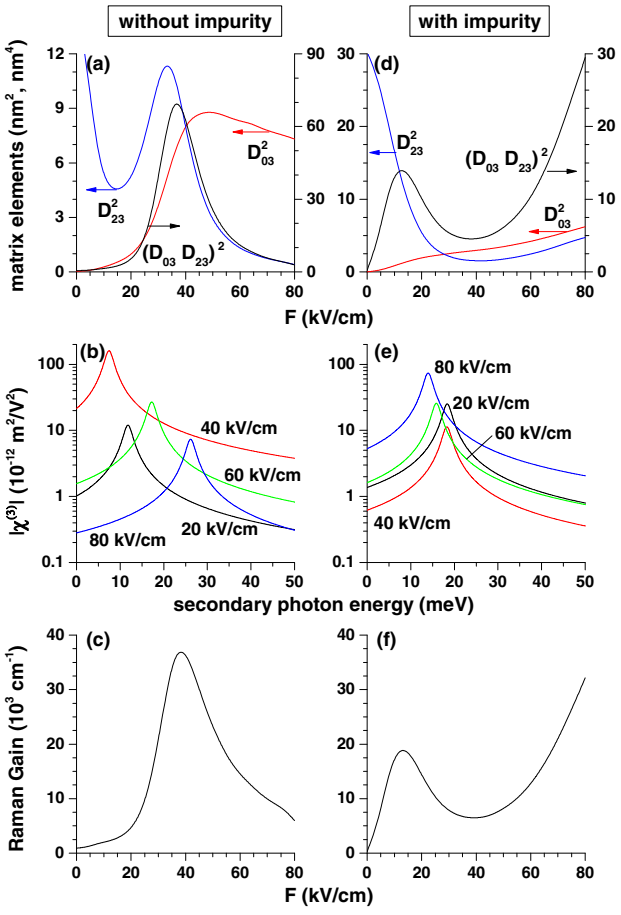


**Fig. 12.** The same as in Figure 11 but with fixed QD size $L = 40$ nm, and electric field as a varying parameter.

about 15 kV/cm but takes maximum magnitude at maximum electric field studied. Maximum magnitudes for both cases are comparable. Further increase of both parameters are expected to remove partially or completely the confinement of the upper involved state and so to pull out the system from the range of applicability of our model. This means that in order to reach a stable Raman gain, the case without ionized impurity looks preferable.

## 4 Conclusions

In this article we have theoretically studied the electron-related Raman scattering and Raman gain in GaAs/AlGaAs triangular quantum dots with all process taking place within the conduction band. Our discussion has highlighted the influence on these properties of the quantum dot size, the presence or absence of an ionized donor impurity center placed at the orthocenter of the triangle as well as of a external DC electric field applied in the quantum dot plane. We found that the applied electric field along one of the triangle symmetry axis changes the symmetry of the system that leads to the exchange of energy positions of second and third excited size-confined states under large enough electric field conditions. Besides, it is revealed that the size of quantum dot amplifies this effect and the presence of the ionized impurity center weakens it. Based on that analysis we described the most favorable conditions to obtain Raman emission and gain under the described conditions. Values of the Raman gain of the order of $10^3\,\mathrm{cm}^{-1}$ are foreseeable thus giving this kind of low-dimensional nanostructures a prospective application in inter-state Raman optical devices.

## Author contribution statement

All authors contributed equally to the paper.

The authors are grateful to the Colombian Agencies CODI-Universidad de Antioquia (Estrategia de Sostenibilidad de la Universidad de Antioquia and project: "*Manipulación de propiedades optoelectrónicas de nanoestructuras*

*semiconductoras por ondas acústicas superficiales*"), Facultad de Ciencias Exactas y Naturales-Universidad de Antioquia (CAD and ALM-exclusive dedication projects 2015-2016), and El Patrimonio Autónomo Fondo Nacional de Financiamiento para la Ciencia, la Tecnología y la Innovación, Francisco José de Caldas.

## References

1. C.Y. Ngo, S.F. Yoon, W.J. Fan, S.J. Chua, Phys. Rev. B **74**, 245331 (2006)
2. E. Giraldo-Tobón, W. Ospina, G.L. Miranda-Pedraza, M.E. Mora-Ramos, Superlattice Microstruct. **83**, 157 (2015)
3. S.H. Gong, J.H. Kim, Y.H. Ko, C. Rodriguez, J. Shin, Y.H. Lee, L.S. Dang, X. Zhang, Y.H. Cho, Proc. Natl. Acad. Sci. **112**, 5280 (2015)
4. T. Kumagai, A. Tamura, J. Phys.: Condens. Matter **20**, 285220 (2008)
5. J. Nelayah, L. Gu, W. Sigle, C.T. Koch, I. Pastoriza-Santos, L.M. Liz-Marzán, P.A. van Aken, Opt. Lett. **34**, 1003 (2009)
6. H.Y. Xu, Z. Liu, Y. Liang, Y.Y. Rao, X.T. Zhang, S.K. Hark, Appl. Phys. Lett. **95**, 133108 (2009)
7. M. Jo, T. Mano, M. Abbarchi, T. Kuroda, Y. Sakuma, K. Sakoda, Cryst. Growth Des. **12**, 1411 (2012)
8. M. Jo, T. Mano, M. Abbarchi, T. Kuroda, K. Sakoda, AIP Conf. Proc. **1598**, 71 (2014)
9. G. Eckhardt, R.W. Hellwarth, F.J. McClung, S.E. Schwarz, D. Weiner, E.J. Woodbury, Phys. Rev. Lett. **9**, 455 (1962)
10. K.O. Hill, B.S. Kawasaki, D.C. Johnson, Appl. Phys. Lett. **29**, 181 (1976)
11. M.A. Ferrara, I. Rendina, L. Sirleto, in *Nonlinear Optics* (InTech, Croatia, 2012), pp. 53–70
12. J.M. Elzerman, K.M. Weiss, J. Miguel-Sanchez, A. Imamoğlu, Phys. Rev. Lett. **107**, 017401 (2011)
13. R. Heitz, H. Born, A. Hoffmann, D. Bimberg, I. Mukhametzhanov, A. Madhukar, Appl. Phys. Lett. **77**, 3746 (2000)
14. A. Tiutiunnyk, V. Tulupenko, M.E. Mora-Ramos, E. Kasapoglu, F. Ungan, H. Sari, I. Sökmen, C.A. Duque, Physica E **60**, 127 (2014)
15. A. Tiutiunnyk, V. Tulupenko, V. Akimov, R. Demediuk, A.L. Morales, M.E. Mora-Ramos, A. Radu, C.A. Duque, Superlattice and Microstruct. **87**, 131 (2015)
16. N. Ha, T. Mano, Y.-L. Chou, Y.-N. Wu, S.-J. Cheng, J. Bocquel, P.M. Koenraad, A. Ohtake, Y. Sakuma, K. Sakoda, T. Kuroda, Phys. Rev. B **92**, 075306 (2015)
17. W.-K. Li, S.M. Blinder, J. Math. Phys. **26**, 2784 (1985)
18. F. Comas, C. Trallero Giner, R. Pérez-Alvarez, J. Phys. C **19**, 6479 (1986)
19. R. Enderlein, Phys. Stat. Sol. B **70**, 263 (1975)
20. I.G. Lang, S.T. Pavlov, A.V. Prokaznickov, A.V. Goltsev, Phys. Stat. Sol. B **127**, 187 (1985)
21. R. Riera, J.L. Marín, R.A. Rosas, in *Handbook of Advanced Electronic and Photonic Materials and Devices*, edited by H.S. Nalwa (Academic Press, New York, 2001), Vol. 6, pp. 1–117
22. R. Betancourt-Riera, R. Riera, J.L. Marín, R. Rosas, in *Encyclopedia of Nanoscience and Nanotechnology*, edited by H.S. Nalwa (American Scientific Publishers, Valencia, 2003), Vol. 3, pp. 101–137
23. M.J. Karimi, G. Rezaei, H. Pakarzadeh, Phys. Lett. A **377**, 2164 (2013)
24. J.B. Khurgin, G. Sun, L.R. Friedman, R.A. Soref, J. Appl. Phys. **78**, 7398 (1995)
25. I. Vurgaftman, J.R. Meyer, L. R. Ram-Mohan, J. Appl. Phys. **89**, 5815 (2001)
26. H. Sun, S.-W. Gu, Commun. Theor. Phys. **17**, 229 (1992)
27. M.E. Reimer, M. Korkusiński, D. Dalacu, J. Lefebvre, J. Lapointe, P.J. Poole, G.C. Aers, W.R. McKinnon, P. Hawrylak, R.L. Williams, Phys. Rev. B **78**, 195301 (2008)
28. T. Nakaoka, Y. Tamura, T. Saito, T. Miyazawa, K. Watanabe, Y. Ota, S. Iwamoto, Y. Arakawa, Appl. Phys. Lett. **99**, 181109 (2011)
29. V. Stavarache, D. Reuter, A.D. Wieck, M. Schwab, D.R. Yakovlev, R. Oulton, M. Bayer, Appl. Phys. Lett. **89**, 123105 (2006)
30. M. Scheinert, H. Sigg, S. Tsujino, M. Giovannini, J. Faist, Appl. Phys. Lett. **91**, 131108 (2007)
31. O. Gauthier-Lafaye, P. Boucaud, F.H. Julien, S. Sauvage, S. Cabaret, J.-M. Lourtioz, V. Thierry-Mieg, R. Planel, Appl. Phys. Lett. **71**, 3619 (1997)
32. G. Sun, J.B. Khurgin, L. Friedman, R.A. Soref, J. Opt. Soc. Am. B **15**, 648 (1998)